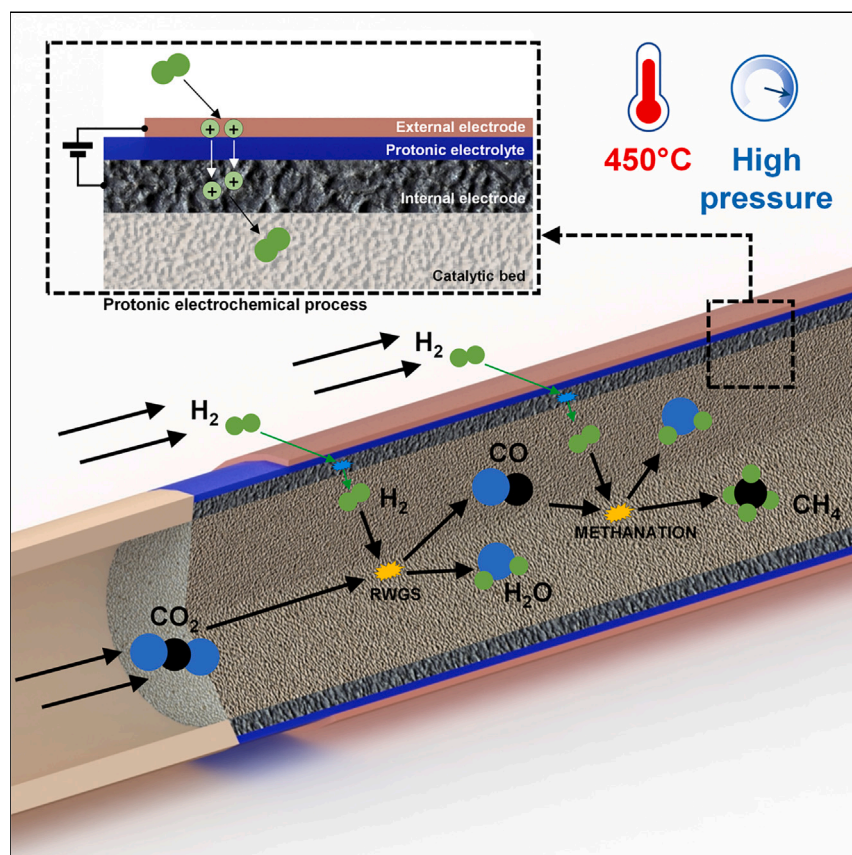


Article

Direct electrocatalytic CO₂ reduction in a pressurized tubular protonic membrane reactor



Imanol Quina, Laura Almar, David Catalán-Martínez, ..., Truls Norby, Sonia Escolástico, Jose M. Serra

soesro@itq.upv.es (S.E.)
jmserra@itq.upv.es (J.M.S.)

Highlights

Protonic electrochemical cells operated at 450°C and 30 bar enabled CO₂ methanation

Pressurized proton pumping and Ni-based electrocatalysis led to CH₄ yields >99%

High-pressure operation and CO₂-rich atmosphere boosted electrochemical performance

Energy storage is crucial for transitioning from fossil fuels to sustainable resources. Converting intermittent electricity into chemical carriers like hydrocarbons eases storage and transport. Sustainable methane generated from electricity leverages existing natural gas infrastructure, serving as energy storage and a decarbonization solution for transport and industry. In methane synthesis, integration of hydrogen production and CO₂ conversion in a single step will lead to higher energy efficiency. Here, a pressurized, electrochemically driven reactor transformed CO₂ into methane with yields greater than 99%.



Quina et al., Chem Catalysis 3, 100766
October 19, 2023 © 2023 The Authors.
Published by Elsevier Inc.
<https://doi.org/10.1016/j.cheecat.2023.100766>



Article

Direct electrocatalytic CO₂ reduction in a pressurized tubular protonic membrane reactorImanol Quina,¹ Laura Almar,¹ David Catalán-Martínez,¹ Amir Masoud Dayaghi,² Agustín Martínez,¹ Truls Norby,² Sonia Escolástico,^{1,*} and Jose M. Serra^{1,3,*}

SUMMARY

Power-to-methane technology enables storage of renewable electricity in chemical energy, which can be transported and converted using existing infrastructure. The moderate energy efficiency of this process is associated with high reactor exothermicity and complex thermal integration. Proton-ceramic electrochemical cells (PCECs) enable thermal combination of methanation and electrochemically driven H₂ steps via endothermic reactions, boosting energy efficiency and heat management. Here, we report single-step methane production from CO₂ in a tubular PCEC at 450°C and less than 30 bar. The H₂ reactant is supplied by electrochemical pumping of protons from H₂ in the external chamber. The electrochemical cell consists of an ~25-μm-thick electrolyte (BaZr_{0.8}Ce_{0.1}Y_{0.1}O_{3-δ}) supported on a BaZr_{0.8}Ce_{0.1}Y_{0.1}O_{3-δ}/Ni composite acting as a methanation catalyst. The reaction was studied as a function of total pressure, H₂/CO₂ ratio, and current density, reaching CH₄ yields greater than 99% above 20 bar. High pressure and a CO₂-rich atmosphere ameliorated the electrochemical behavior because of higher electrolyte hydration and boosted electrode kinetics.

INTRODUCTION

Nowadays, more than 80% of our energy demand is covered by fossil fuels—mainly crude oil, coal, and natural gas.¹ The continuous rise in world population coupled with an increasing global energy demand has led to extensive use of fossil fuels, which has two main problems: (1) fossil fuels are limited and not renewable, and (2) CO₂ emissions from the combustion process contribute to global warming. These aspects highlight the importance of developing an alternative technology for CO₂-free power generation.² Renewable energy sources like solar and wind energy are bound to take over,³ but the fluctuating nature of such renewable sources makes it difficult to balance the energy produced and consumed. Solutions to couple the energy demand with the energy produced are hence vital to ensure a stable energy supply.^{1,3–5} In recent years, incorporating energy storage systems into the electricity grid has been chosen as one of the most credible solutions. The current solutions mainly include pumped-storage hydropower plants, batteries, flywheels, and compressed air energy storage. Each of these technologies has its own advantages and disadvantages, but none offers a solution on a sufficient scale yet. Another promising alternative is power-to-gas technology,^{3,6,7} which consists of conversion of electricity into gas chemical energy carriers such as hydrogen, methane, or ammonia. This concept allows storage of energy in the form of chemical energy, which is reconverted into electricity when required. Regarding power-to-hydrogen technology, the main challenges that need to be faced are its low volumetric energy density, the need for solutions to achieve safety and reduced cost for its transport,

THE BIGGER PICTURE

Transformation of intermittent electric power into chemical carriers like NH₃ and hydrocarbons will facilitate energy storage and transport. Sustainable methane produced from electricity can utilize the existing infrastructure for distribution and large-capacity energy storage. Carbon-neutral methane can be used in current production processes, supporting progressive decarbonization of transport and industry. In methane synthesis, integration of hydrogen production (e.g., by water electrolysis) and CO₂ hydrogenation in a single step will lead to higher energy efficiency. Here, we propose a pressurized, electrochemically driven reactor that can transform CO₂ into methane and integrates a protonic ceramic membrane that can extract protons from H₂ or H₂O and inject the protons. The reactor at 450°C produced a methane stream at 30 bar with yields greater than 99%, illustrating the potential of process intensification for catalytic conversion of CO₂ in electrified reactors.



and its limited compatibility with the existing infrastructure.⁸ On the other hand, power-to-methane technology is often preferred because it can be used directly with the existing natural gas infrastructure.⁹

Power-to-methane technology is based on a two-step process: hydrogen production via steam or water electrolysis and subsequent CO₂ methanation to produce methane. Electrochemical water splitting is a well-known technology that can be performed at low and high temperatures (Equation 1):¹⁰



CO₂ methanation is an exothermic process with a volume decrease composed of different reactions, mainly CO₂ methanation (Sabatier reaction [Equation 2], CO methanation [Equation 3], and reverse water gas shift [RWGS] reaction [Equation 4]). Then, to promote CH₄ formation, and according to Le Chatelier's principle, CO₂ methanation should be performed at low temperature (typically between 200°C and 400°C¹¹) and high pressure. High temperature shifts the equilibrium toward reactants, decreasing CO₂ conversion and favoring CO production via the RWGS reaction.^{10,12,13} In addition, high pressure improves reactant conversion and, subsequently, CH₄ yield. The H₂/CO₂ ratio is another parameter affecting the performance of the reaction. Different studies proved that H₂/CO₂ ratios between 4 and 7 (above the stoichiometric ratio) improve CO₂ conversion and prevent coke formation.^{13,14}

To improve the performance of the CO₂ methanation reaction, because a low temperature favors the thermodynamics of the reaction but limits the kinetics, many catalysts have been developed over the last few years. These catalysts are typically based on active metal particles (Ni, Fe, Rh, Co, Pt, W, or Mo) dispersed on metal-oxide supports (Al₂O₃, SiO₂, or TiO₂):¹⁵



One of the main drawbacks of power-to-methane technologies is that, currently, they are not economically competitive compared with natural gas, mainly because of the high cost of H₂ production by electrolysis.¹⁶ The CO₂ methanation reaction can be carried out by applying different technologies, such as thermocatalysis, photocatalysis, electrocatalysis, and biocatalysis. Thermocatalysis is a mature technology and one of the most common forms of catalysis because of its high efficiency and applicability to industrial processes. At low temperatures, CO₂ can be hydrogenated to produce CH₄ by photocatalysis, electrocatalysis, and plasma catalysis, but these technologies are still immature, and CH₄ selectivity and efficiency should be improved.^{17–19} Regarding the mechanism of CH₄ production via CO₂ reduction with H₂ over heterogeneous catalysts, extensive theoretical and experimental works have been published.^{20–22} It has been reported that CO₂ hydrogenation follows the next route on Ni-based catalysts:²³ CO₂* activation (where * refers to adsorbed intermediate species) forms CO* and O*, then the smallest-barrier and lowest-energy pathways for surface-catalyzed CO* transformation proceed through HCO*, and thereafter, different elementary steps that include formation of CH₂* can be followed. Formation of HCO* has been identified as the rate-limiting step (RLS) of CH₄ formation by a microkinetics model.²⁴ On the other hand, the same study reports that the selectivity of catalytic CO₂ conversion into CO and CH₄ on transition metals such as Pt, Pd, Ni, Rh, and Ru can correlate with the oxygen binding energy: weaker

¹Instituto de Tecnología Química, Universitat Politècnica de València – Consejo Superior de Investigaciones Científicas, Av. Los Naranjos, s/n, 46022 Valencia, Spain

²Department of Chemistry, University of Oslo, Centre for Materials Science and Nanotechnology, Gaustadalléen 21, 0349 Oslo, Norway

³Lead contact

*Correspondence: soesro@itq.upv.es (S.E.), jmserra@itq.upv.es (J.M.S.)

<https://doi.org/10.1016/j.checat.2023.100766>

oxygen binding metals only converted CO₂ mildly to CO, as is the case for Pt and Pd, whereas for Ni, Rh, and Ru with stronger oxygen binding, higher conversion to CH₄ is obtained. In the same microkinetics model, it was deduced that higher H* surface coverage is obtained with higher temperatures and p_{H₂}, which improves the CH₄ production rate. In contrast, higher CO₂* coverage leads to lower rates. Therefore, working at higher temperatures and local p_{H₂} favors CH₄ production.

In recent years, power-to-methane technology has been coupled with solid oxide electrolysis cells (SOECs). This concept is based on process intensification, joining steam electrolysis and the methanation reaction in a single-step process.²⁵ Heat integration between the exothermic (methanation reaction) and endothermic (steam electrolysis) processes leads to higher energy efficiency.²⁶ Conventional oxygen-ion conduction-based SOECs require operation at 650°C–900°C because of the low ionic conductivity of the electrolytes, such as yttria-stabilized zirconia, at lower temperatures. High temperatures cause operational problems related to the lifetime and degradation of the stack components²⁷ in addition to low methane yields.^{28,29} Proton-ceramic electrolysis cells (PCECs) are good candidates to overcome these limitations because of their higher ionic conductivity at intermediate temperatures (400°C–650°C),³⁰ enabling operation at lower temperatures and, thus, favoring the methanation reaction.³¹ Over the last years, proton-conducting ceramic membranes have been studied for many applications, such as hydrogen pumping,^{32–36} methane conversion into aromatics,³⁷ or intensified steam-methane reforming at high pressure.^{26,38}

Different works on power-to-methane applications at atmospheric pressure using PCECs have been published recently. Xie et al.³⁹ used a planar membrane based on BaCe_{0.5}Zr_{0.3}Y_{0.16}Zn_{0.04}O_{3-δ} as an electrolyte to produce CH₄ from CO₂ and H₂ (provided by hydrogen pumping), reaching a methane and CO production rate of 0.07 mL min⁻¹ cm⁻² and 3.25 mL min⁻¹ cm⁻², respectively, at 614°C. On the other hand, CH₄ production by CO₂ and H₂O co-electrolysis using BaCe_{0.7}Zr_{0.1}Y_{0.1}Yb_{0.1}O_{3-δ} and BaCe_{0.4}Zr_{0.4}Y_{0.1}Yb_{0.1}O_{3-δ} has also been studied, reaching a methane yield of 7.5% at 500°C applying -1.625 A (0.5 cm² active area) and of 34.6% at 450°C, respectively.^{27,40}

To the best of our knowledge, pressurized methanation production combined with solid-oxide electrochemical cells has not been reported. Tubular cells have the advantage of being able to operate at high pressure as well as with large pressure differences between the two chambers, as proven in previous studies.^{26,38,41} In this work, direct CO₂ conversion into CH₄ mediated by electrochemically driven H₂ pumping in a 16-cm² tubular protonic membrane is performed at pressures up to 30 bar and 450°C. The catalytic and electrochemical performance of the protonic cells is evaluated by current density-voltage (i-V) curves and impedance spectroscopy analysis in coupled H₂-pumping and methanation operation. The performance of electrochemical cells is boosted under pressurized conditions as a result of the higher proton conductivity because of the higher partial pressure of H₂O (and the associated electrolyte hydration degree) and the improved surface kinetics and mass transport of the electrodes. CO₂ conversion and CH₄ and CO selectivity are investigated as a function of the total pressure, H₂/CO₂ ratio, and the CO₂ feed flow rate.

RESULTS AND DISCUSSION

Cell performance and pressure effect in H₂ pumping mode

The methanation reaction occurs following Equation 2, and depending on the H₂/CO₂ ratio, temperature, and pressure, CO formation is also expected by the

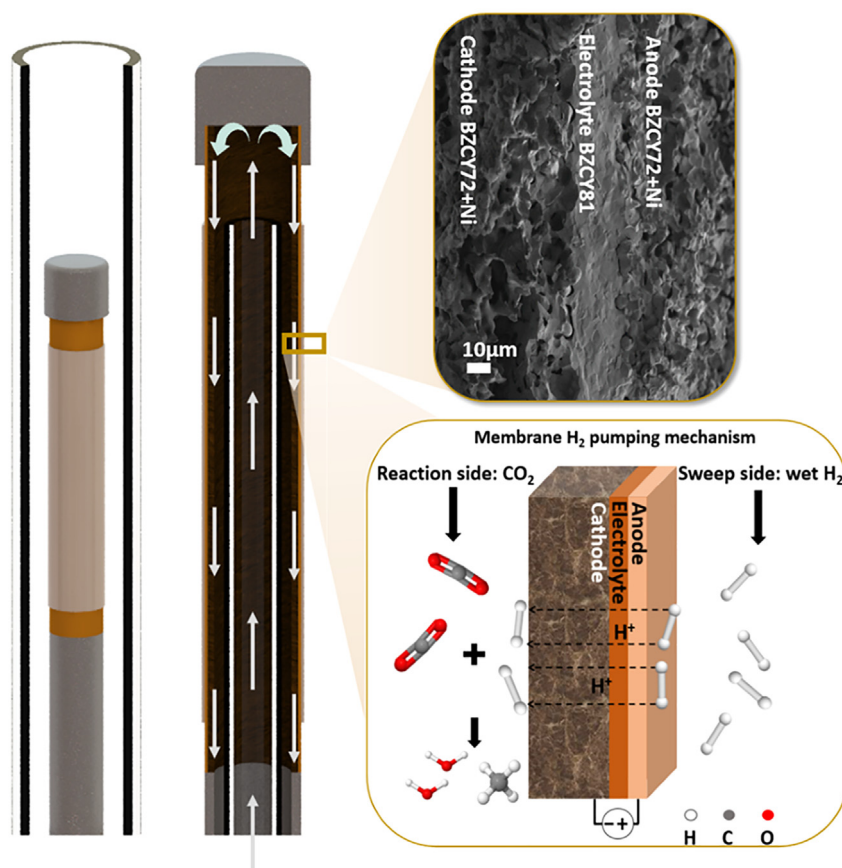


Figure 1. Electrochemical reactor architecture and operation

Shown are schematics of the reactor configuration for the methanation reaction. Top: SEM image of the membrane assembly comprising the microstructure of the cathode Ni-BZCY72/electrolyte BZCY81/anode Ni-BZCY72. Bottom: H₂ pumping mechanism and chemical and electrochemical reactions.

RWGS reaction (Equation 4). In this work, CO₂ is fed in the reaction chamber (internal chamber), whereas H₂ is fed in the external chamber. The H₂ needed for the methanation reaction was obtained by H₂ pumping, as shown in Figure 1. This mimics the intensified methanation process, where protons are extracted either from water via steam electrolysis or from an H₂-bearing industrial waste stream. The H₂ injected by pumping protons into the reaction chamber reacts with the CO₂, producing CH₄. The internal Ni-based electrode acts as a catalyst for the methanation reaction.

First, the electrochemical properties of the cells were characterized at 450°C and pressures ranging from 1–30 bar feeding a humidified gas stream (2.5% H₂O) composed of 40 mL min⁻¹ of H₂ and 30 mL min⁻¹ of N₂ in the outer chamber and dry 10 mL min⁻¹ of H₂ and 80 mL min⁻¹ of N₂ in the reaction chamber. Figures 2A and 2C show the electrochemical impedance spectroscopy (EIS) spectra obtained as a function of the pressure and the corresponding distribution of the relaxation time (DRT), respectively. Three different contributions at 2.5–5 × 10⁻⁴, 7–9 × 10⁻³, and 4–8 × 10⁻¹ s can be observed up to 5 bar, while at higher pressures, the contribution around 5 × 10⁻¹ s is eliminated. The latter can be attributed to gas diffusion because of its strong pressure dependency and high time constant (low frequency).^{43,44} The resistance of the peaks at 2.5–5 × 10⁻⁴ and 7–9 × 10⁻³ s decreases with system pressurization, but the time constants (τ)

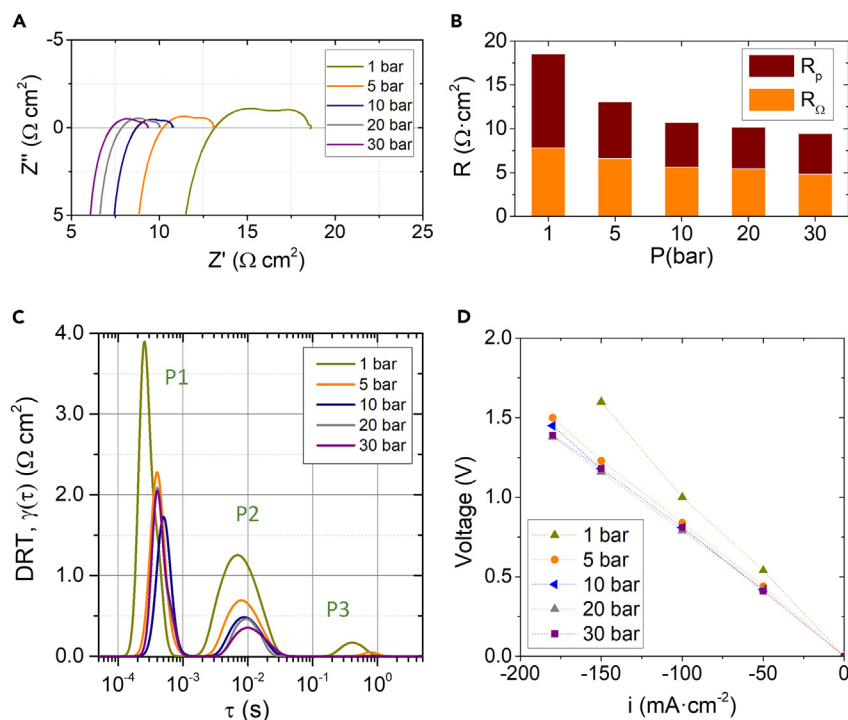


Figure 2. Characterization of the proton-pumping operation

(A) EIS spectra at 450°C and different operation pressures (from 1–30 bar).

(B–D) Ohmic and polarization resistance extracted from the EIS fittings (B), corresponding DRT analysis (C), and i-V curves (D).

In all measurements, a humidified (2.5% H₂O) atmosphere composed of 10 mL min⁻¹ H₂ and 80 mL min⁻¹ N₂ was fed to the inner chamber, and a mixture of 40 mL min⁻¹ H₂ and 30 mL min⁻¹ N₂ was fed to the outer chamber.

increase and remain nearly constant, respectively. We attribute this to the increased capacitance associated with a higher charge-carrier concentration on the electrode surface and/or a higher surface coverage of charged adsorbates. Based on the DRT analysis, the impedance spectra were fitted with the equivalent circuit LR₀(R₁CPE₁)(R₂CPE₂)(R₃CPE₃) and LR₀(R₁CPE₁)(R₂CPE₂) depending on the pressure, where 1, 2, and 3 correspond to peaks P1, P2, and P3 in Figure 2C. The capacitance associated with P1 and P2 ranges from 3–6.8 × 10⁻⁶ F cm⁻² and 5.5 × 10⁻³ to 6.8 × 10⁻² F cm⁻², respectively, in agreement with the shift observed in the DRT analysis. The capacitance associated with P3 was around 1.6 F cm⁻², typical for mass transport processes within the electrode. Figure 2B shows the ohmic and polarization resistance as a function of the total pressure obtained from fitting of the EIS spectra. Ohmic and polarization resistance decrease with pressurization of the electrochemical cell. The polarization resistance is improved significantly from 10.7 Ω cm² at 1 bar to 4.6 Ω cm² at 30 bar. The decrease in ohmic resistance is related to the higher protonic conductivity of the electrolyte because of the higher pH₂O under pressurized conditions. This improvement with increasing pressure allows working at higher current densities, and, indeed, the lower voltage reached is consistent with the polarization behavior shown in Figure 2D. By applying a voltage of 1.2 V, the tubular cell worked at a current density of -155 mA cm⁻² at 30 bar, whereas at atmospheric pressure, it decreased to -115 mA cm⁻².

In summary, the improvement of the cell performance under pressurized operation can be ascribed to two different phenomena: (1) higher partial pressure of H₂O

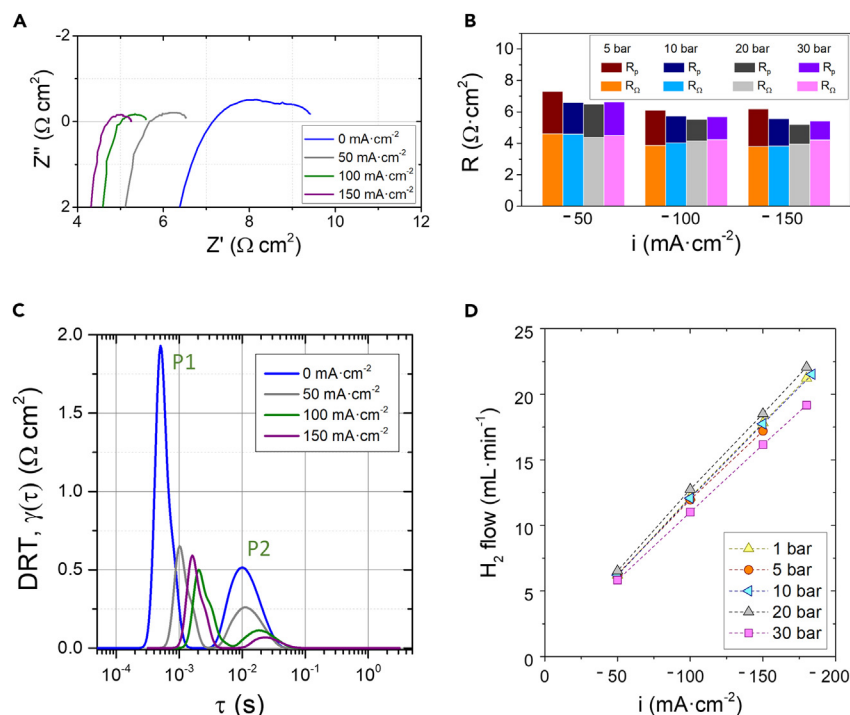


Figure 3. Analysis of resistive contributions in electrochemical proton pumping

(A and C) Nyquist plot (A) and the corresponding DRT analysis (C) as a function of the applied current density at 450°C and 30 bar during the H₂ pumping tests.

(B and D) Fitted ohmic and polarization resistance (B) and H₂ flow (D) as a function of the pressure and applied current density.

For all the measurements, 80 mL min⁻¹ N₂ was fed in the inner chamber and a humidified (2.5% of H₂O) atmosphere composed of 40 mL min⁻¹ H₂ and 30 mL min⁻¹ N₂ in the outer chamber.

leading to higher electrolyte hydration and protonic conductivity and (2) improvement of the surface kinetics and mass transport of the electrodes that give rise to lower polarization resistance.

For quantification of H₂ pumping through the electrolyte and evaluation of the faradic efficiency, the reaction chamber feed was changed to 80 mL min⁻¹ of dry N₂. Figure 3D plots H₂ pumping from the outer chamber to the inner chamber as a function of pressure (from 1–30 bar) and applied current density (up to –180 mA cm⁻²). The plotted values are the average of the H₂ flow obtained during 30 min when applying a constant current density (pumping step). An H₂ flow of 22 mL min⁻¹ was obtained at the maximum applied current density. In addition, ~100% faradic efficiency was reached under all conditions. The faradic efficiency (η_F ; Equation 5) was calculated from the theoretical H₂ production defined in Equation 6 ($F(H_2)_{th}$), where n is the number of transferred electrons and F the Faraday constant and the obtained H₂ flow quantified by gas chromatography $F(H_2)_{exp}$:

$$\eta_F = \frac{F(H_2)_{exp}}{F(H_2)_{th}} \quad (\text{Equation 5})$$

where

$$F(H_2)_{th} = \frac{I}{nF} \quad (\text{Equation 6})$$

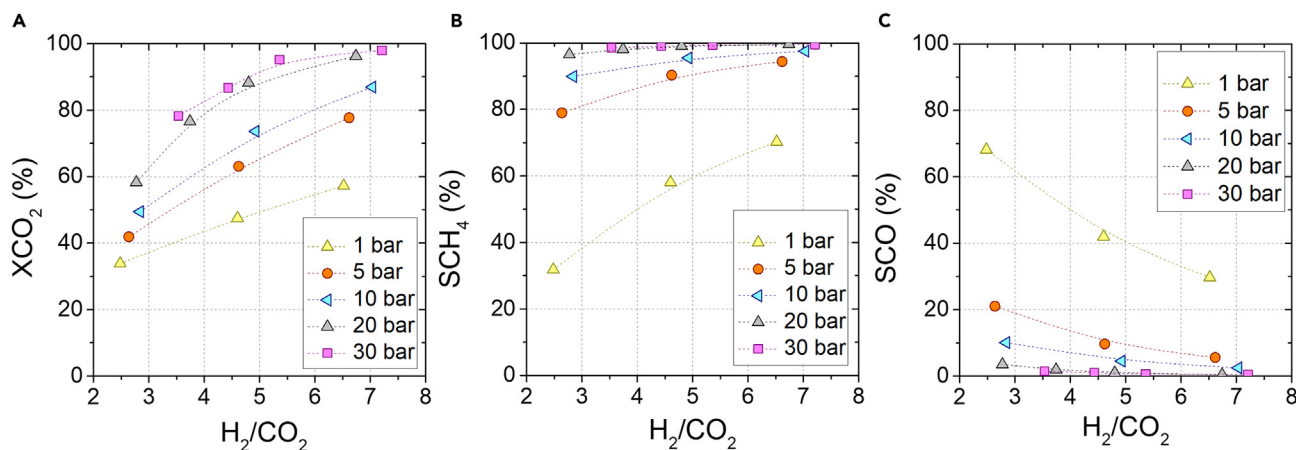


Figure 4. Methanation performance in the electrochemical reactor

(A–C) CO₂ conversion (A) and CH₄ (B) and CO selectivity (C) as a function of the pressure and the H₂/CO₂ ratio at 450°C. Dry 150 mL min⁻¹ of an atmosphere composed of 2% CO₂ and 4% He diluted in Ar were fed in the reaction chamber.

The electrochemical performance of the cell was also evaluated during the H₂ pumping experiments, with EIS measurements performed at the end of each step. Figures 3A and 3C show the EIS spectra obtained as a function of the applied current density and the corresponding DRT at 30 bar, respectively. Two different contributions are observed at 30 bar, in agreement with the results shown in Figure 2C. The peaks shift to a higher time constant, and resistance decreases when increasing the applied current density, indicating an increase in the capacitance of the two processes. The associated capacitance shifts from 6.7×10^{-6} to 5.2×10^{-5} F cm⁻² and from 2.2×10^{-2} to 6.9×10^{-2} F cm⁻² for P1 and P2, respectively. This increase is associated with surface-related effects; i.e., a higher charge carrier and/or charged adsorbate concentration on the electrode surface.⁴⁵ The same behavior, a decrease in resistance with the applied current density, is also observed for the rest of the pressures studied, as shown in Figures 3A and 3B.

Cell performance in the methanation reaction

The methanation reaction was evaluated at 450°C, feeding CO₂ (3 mL min⁻¹) in the reaction chamber and controlling the H₂/CO₂ ratio by varying the applied current density. Figure 4 plots the CO₂ conversion (Figure 4A) and the selectivity to CH₄ (Figure 4B) and CO (Figure 4C) as a function of pressure and the H₂/CO₂ ratio obtained in the reaction chamber. The plotted values are the average of all data obtained at steady state (at least 50 min on stream). The molar flow rates obtained in the reaction are given in Tables S3–S9 for the different conditions evaluated. It is observed that the higher the pressure, the better the performance, as postulated by Le Chatelier's principle, improving CO₂ conversion and CH₄ yield. The CO₂ conversion increases from 45% to 86% with a stoichiometric H₂/CO₂ ratio of 4 when the pressure increases from 1 to 30 bar. CH₄ selectivity increases from 50% at 1 bar to greater than 99% at 30 bar. The most significant improvement is observed between 1 and 5 bar, where CH₄ selectivity rises from 50% to 85%. On the other hand, the reaction performance improves with the H₂/CO₂ ratio, as reported previously, because it increases CO₂ conversion and prevents coke formation.^{13,14} This improvement comes at the expense of increasing the process operating cost related to the higher electric currents and downstream separation. Therefore, the H₂/CO₂ ratio can be adjusted by applying different current densities to achieve the best operating conditions in terms of performance and cost. Coke formation was calculated by carbon mass balance,

and coke production was only detected at low H_2/CO_2 ratios (below 3), with the maximum coke selectivity $\sim 15\%$ C at atmospheric pressure. More information on cell performance during the methanation reaction can be found in Figure S2, where CO_2 conversion, CH_4 selectivity, and cell potential at 20 bar are plotted as a function of the applied current density. It should be pointed out that, at -150 mA cm^{-2} , the cell's voltage is below 1.2 V. The methanation reaction was also evaluated with different CO_2 flow rates in the feed (up to 5 mL min^{-1}), obtaining a similar performance as observed in Figure 4. Use of higher CO_2 flow rates was limited by the H_2 flow pumped to maintain the stoichiometric H_2/CO_2 ratio of 4, not by the catalytic activity of the electrode, as inferred from Figure S3.

In addition, the methanation reaction was performed by co-feeding H_2 and CO_2 in the inner chamber of a protonic electrochemical cell (without electrochemical H_2 pumping). Figure S4 shows the comparison between the results obtained in both modes, co-feeding and H_2 pumping at 1 and 5 bar. An improvement of 10 points in the CH_4 yield can be observed when the reaction is performed in H_2 pumping mode. Under the studied conditions, CO_2 reaches the catalytic bed (the internal electrode) by diffusion, and H_2 reaches the electrode by diffusion in co-feeding mode or is generated *in situ* in H_2 pumping. Therefore, the p_{H_2} in co-feeding mode is lower and, consequently, decreases the kinetics reaction.

In this work, the high methanation activity at high pressure in a protonic electrochemical membrane reactor is demonstrated. In addition, the presented methanation reactor provides a solid concept for thermally integrated electrochemical CO_2 conversion and *in situ* separation of gases. In fact, combination of the methanation reaction (exothermic reaction) with an endothermic reaction such as water electrolysis, to provide the H_2 needed in the reaction, in a single electrochemical membrane reactor will lead to efficient energy integration: the heat generated at the exothermic reaction is locally and instantly consumed by the endothermic processes; e.g., water splitting. Hence, heat valorization is optimized, which reduces the need for an external energy supply and causes the entire process to achieve exceptional energy efficiency and process compactness. Finally, to increase CH_4 productivity and make the process viable on an industrial scale, electrochemical cells with larger areas are needed. Fabrication of such cell assemblies on a larger scale has recently been demonstrated.³⁸

Under the practiced conditions, the reaction yield is limited by the thermodynamic equilibrium, as can be inferred from the comparison between the experimental CH_4 yield and that corresponding to the thermodynamic equilibrium (calculated for the same conditions as the testing procedure: 450°C , 20 bar and feeding 2% CO_2) plotted in Figure 5A. Oxide-ion extraction and subsequent H_2O extraction could allow surpassing the CH_4 yield given by the thermodynamic equilibrium.⁴⁶ To evaluate the influence of steam extraction on the reaction, CO was fed instead of CO_2 to mimic a water extraction of 50%. The CH_4 yield strongly increases to 99.7% when CO is fed to the reaction chamber (Figure 5B). A kinetics model of the reaction was built, utilizing experimental results using a fixed-bed reactor using the Ni-based cell's support as catalyst and enables analysis of the elemental steps of the reaction; i.e., absorption and preferred surface reaction pathways. The kinetics model and fitting results are described in Figure S5. The results reveal²³ that the cell's support mechanistically behaves as a conventional Ni-based catalyst despite the much lower surface area of this catalytic support. Namely, CH_4 is produced via hydrogenation of CO_2 or CO (produced by the RWGS reaction). CO hydrogenation is a faster reaction than CO_2 hydrogenation. However, CO production has much lower kinetic

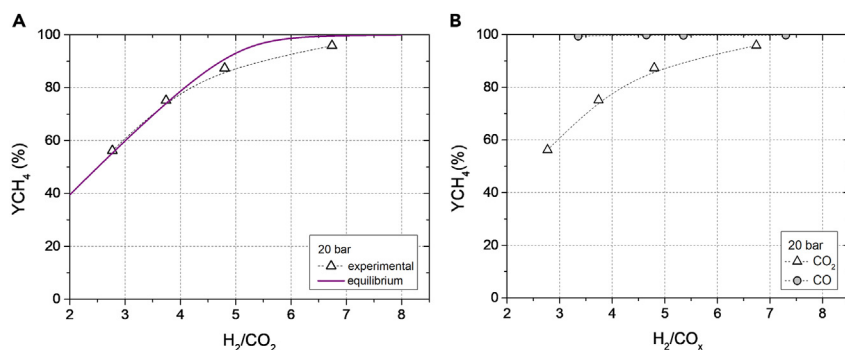


Figure 5. Experimental and (thermodynamic-equilibrium) theoretical CH₄ yield

(A and B) Experimental CH₄ yield feeding CO₂ or CO to the system as a function of the H₂/CO_x ratio at 450°C and 20 bar.

coefficients, which limits the yield of the reaction. Therefore, by extracting oxide ions, CO formation will be promoted and boosts the CH₄ yield in addition to the thermodynamic equilibrium shift triggered by the simultaneous water extraction.

The electrochemical performance of the cell was also evaluated during the methanation reaction at 450°C and 30 bar. Figure 6D shows the i-V curves obtained, showing an improvement of the cell performance under pressurized conditions and compared with the results obtained in H₂ pumping mode (Figure 2D). In fact, current densities of -125 mA cm^{-2} and -160 mA cm^{-2} were reached at 1 bar and 30 bar, respectively, by imposing a voltage of 1.2 V. EIS measurements were performed at the end of each reaction step (after 50 min under steady-state conditions) to evaluate the different transport processes taking place. Figures 6A and 6C show the impedance spectra and corresponding DRT analyses as a function of the applied current density (0/–150 mA cm⁻²). The ohmic and polarization resistance decreases with increasing current density, as shown in Figures 6A and 6B. Two peaks are observed in the DRT analysis, and they shift to higher constant time with increasing applied current density, in agreement with the results shown in Figure 3C, indicating an improvement of the surface exchange kinetics. Figure 6B shows the ohmic and polarization resistance up to 30 bar as a function of the applied current density during H₂ pumping and the methanation reaction. Ohmic and polarization resistance decreases under the methanation reaction compared with the H₂ pumping mode. We attribute the ohmic contribution improvement to steam formation in the methanation reaction, which increases electrolyte hydration, boosting protonic conductivity. As reported, the decrease in polarization resistance is ascribed to the improvement of surface exchange/dissociation and gas diffusion/adsorption caused by the presence of CO₂.⁴⁷

Postmortem analysis

The electrochemical cells were in operation for more than 2 months (>1,500 h) with no significant degradation of electrochemical characterization or reaction performance. After completing all operational tests (including electrochemical characterization, H₂ pumping, and methanation reaction), microstructural analysis of the tubular ceramic membranes was carried out by scanning electron microscopy (SEM). Figure 7 shows cross-sectional SEM images of the postmortem membrane (C2 cell measured up to 30 bar). The cross-sectional image of the interface of the BaZr_{0.8}Ce_{0.1}Y_{0.1}O_{3-δ} (BZCY81) electrolyte and BaZr_{0.7}Ce_{0.2}Y_{0.1}O_{3-δ} and 60 wt % of NiO (Ni-BZCY72) porous electrodes shows good attachment after all measurements

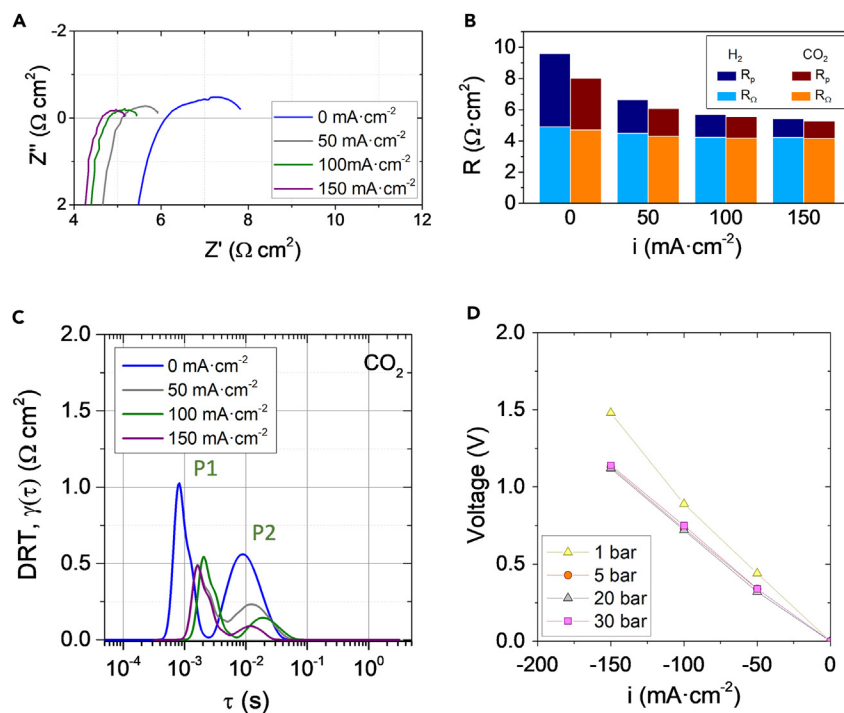


Figure 6. Analysis of resistive contributions in electrochemical methanation operation

(A and C) Nyquist plot (A) and the corresponding DRT analysis (C) as a function of the applied current density at 450°C and 30 bar during the methanation reaction.

(B and D) Ohmic and polarization resistance (B) and i-V curves (D) as a function of the pressure and applied current density.

In all measurements, dry 150 mL min⁻¹ of an atmosphere composed of 2% CO₂ and 4% He diluted in Ar and humidified (2.5% H₂O) 30 mL min⁻¹ N₂ and 40 mL min⁻¹ H₂ were fed in the inner and the outer chamber, respectively.

and electrochemical measurements (Figure 7A). The Ni-BZCY72 external electrode or anode showed a uniform porous thickness of 15 μm; minor agglomeration of nickel was observed, which can be attributed on one hand to the non-optimized dip-coated layer and on the other hand to the long-term test carried out. The dense electrolyte membrane shows a thickness of 25–30 μm. Figure 7C shows the microstructure of the Ni-BZCY72 substrate or cathode where the methanation reaction occurred. The BZCY72 grains show a clean surface, and the nickel grains show a high density of small precipitates (also present in the Ni-BZCY72 cathode but at a lower concentration). Figure 7D shows a larger magnification of a representative nickel particle from the substrate after the methanation tests, where the precipitates and grape-shaped small aggregates of 200–500 nm can be observed (not detectable at the external electrode, as shown in Figure 7B, or in the fresh sample, as shown in Figure S5), which might be related to minor formation of coke at low H₂/CO₂ ratios. Figures 7E–7H show the EDS mapping of the internal electrode after performing all reaction tests. A homogeneous distribution of the two phases (Ni and BZCY72) is observed, and no impurities are detected, indicating integrity of the protonic cell after at least 1,500 h of operation. The stability of the cell structure/microstructure agrees with the stable catalytic activity during the reaction. This stable production can be observed in Tables S3–S9, where the molar flows of CH₄, CO, and CO₂ are listed for the different experiments made with the two different cells. Additional microscopy images for fresh and tested membranes are shown in Figures S6 and S7, respectively). X-ray diffraction (XRD) diffraction measurements were

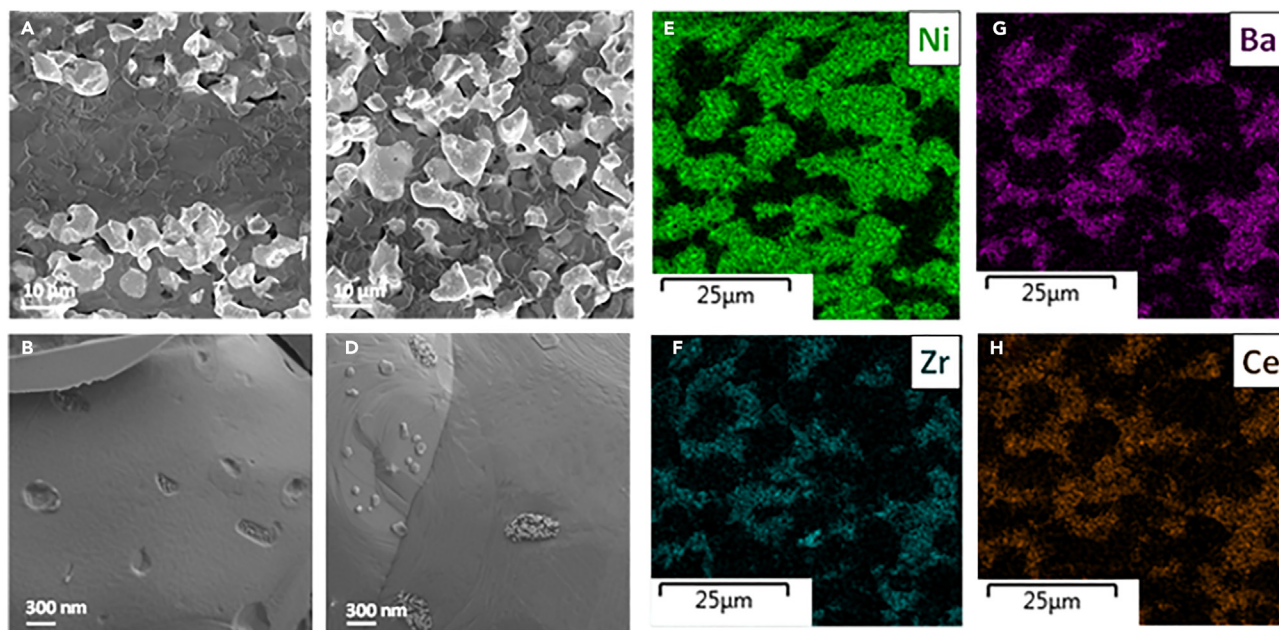


Figure 7. Postmortem SEM cross-sectional analysis of the tubular membranes showing the electrode-electrolyte interface (A–D) External electrode (A) or anode (B), and internal electrode (C) or cathode (D) after performing all reaction tests. (E–H) EDS map of Ni (E), Zr (F), Ba (G), and Ce (H) of the internal electrode after performing all reaction tests.

performed to evaluate the stability of the crystalline structure under the reaction conditions. Figure S8A shows the XRD patterns of a fresh cell and the C2 cell after the measurements. For this analysis, a piece of each tubular cell was ground. No secondary phases related to carbonates or hydroxide species after operation under CO_2 - and H_2O -containing atmospheres were detected, and only peaks related to the Ni and BZCY phase were detected. Note that BZCY phase includes both compositions, BZCY81 and BZCY72 as the cell was ground and the electrodes and electrolyte have different stoichiometry. Rietveld analysis (Figure S8B) was carried out in the C2 cell after the measurements, and the Ni concentration obtained was 65.8 wt %, which is in line with that obtained by X-ray fluorescence (XRF) spectroscopy analysis, 61.2 wt %. Additionally, thermogravimetric measurements were made under an N_2 - CO_2 gas flow for two samples, BZCY72 and BCY10 (as a reference). BZCY72 did not show any sign of carbonation, whereas the cerate BCY10 showed first a typical carbonation process (mass gain from 400°C) and second, above 850°C, a significant mass loss, which is ascribed to carbonate decomposition (Figure S9).

Conclusions

The CO_2 methanation reaction was carried out for the first time in a tubular PCEC at high pressure of up to 30 bar. The H_2 required for CO_2 hydrogenation was supplied by electrochemically pumping H_2 from the external chamber through the protonic electrolyte into the inner reaction chamber. The tubular cell consisted of a BZCY81 electrolyte and metallic electrodes formed by Ni-BZCY72. The BZCY72-Ni of the inner cathodic support also acted as a methanation catalyst. The H_2/CO_2 ratio in the reaction was controlled by the applied current density. The protonic cell reactor was electrochemically characterized by i-V curves and impedance spectroscopic analyses in H_2 pumping and methanation modes. The pressurized operation enabled improvement of the methanation performance in both modes, and this is attributed to (1) the higher steam partial pressure, enhancing hydration of the

ceramic electrolyte and, consequently, boosting protonic conduction, and (2) promotion of the electrode surface kinetics by increasing the surface coverage of reacting and intermediate species, as inferred from DRT analysis. The methanation yield is strongly influenced by total pressure and H₂/CO₂ ratio. Pressurization of the cell led to a notable rise in CH₄ yield, reaching values of ~80% at 20 bar at the stoichiometric H₂/CO₂ ratio of 4, in line with the thermodynamic equilibrium yield. To further boost the methanation yield, the *in-situ* extraction of the water was mimicked by feeding CO instead of CO₂, reaching CH₄ yield values close to 100%, highlighting the paramount importance of the water extraction function in the CO₂ methanation reaction. Notably, no performance degradation was observed in either the catalytic or electrochemical properties of the protonic cell reactor after at least 1,500 h of operation. These results evidence the great potential of tubular PCECs in intensification of CO₂ hydrogenation processes, allowing high-pressure operation with high reaction yields and heat integration. The proposed concepts will enable coupling of the CO₂-to-methane reaction with either water electrolysis or H₂ recovery from industrial streams.

EXPERIMENTAL PROCEDURES

Resource availability

Lead contact

Further information and requests for resources should be directed to and will be fulfilled by the lead contact, Jose M. Serra (jmserra@itq.upv.es).

Materials availability

This study did not generate new materials.

Data and code availability

There is no dataset or code associated with this publication. All relevant experimental data and procedures are provided in the main article and the supplemental information.

Fabrication of tubular ceramic membranes

Tubular ceramic protonic membranes were prepared by sintering a coated and extruded substrate as support.^{26,38} The extruded supports consist of a mixture of ceramic powders, with BaSO₄, CeO₂, ZrO₂, and Y₂O₃ as precursors; NiO as a sintering aid; and an aqueous binder system (aqueous methylcellulose [Methocel E10M, DuPont], starch [Redisol, Tate & Lyle], and polyethylene glycol as rheology modifier [PEG400, Sigma-Aldrich]). The molar ratios between the precursors were fixed to produce BaZr_{0.7}Ce_{0.2}Y_{0.1}O_{3-δ} (BZCY72). After that, the precursors' mixture was blended with the NiO (IP Grade, Sumitomo) to obtain the extruded composition of 40 wt % of Ni-BZCY72. After extrusion of the mixture, the ceramic segments were dried for 24 h, and the electrolyte was spray coated using a slurry composed of binders and organic solvent (methyl methacrylate binder [Elvacite 2927, Mitsubishi Chemical], pentyl acetate organic solvent [Sigma-Aldrich], and terpineol as a rheological additive [Sigma Aldrich]) and a stoichiometric mixture of BaSO₄, CeO₂, ZrO₂, and Y₂O₃ to yield BZCY81. The outer electrode was applied by dip coating using a slurry with the same composition as the extruded mixture (Ni-BZCY72). Then, the ceramic tubes were sintered at 1,610°C for 15 h in a furnace to densify the sample fully. Then the tubular cell was treated at 1,000°C for 24 h in a flow of 5% H₂ to reduce nickel oxide. Finally, each ceramic segment was sealed to a cap and a riser on the respective sides using ceramic glass sealings. A schematic of the tubular membranes and a typical SEM cross-section image are shown in Figure 1. The ceramic segment sealed to the cap and riser is

depicted as three-cell components (support Ni-BZCY72/electrolyte BZCY81/outer electrode Ni-BZCY72).

Reactor setup

The set-up consisted of an external tubular steel shell with a VCR®-Swagelok-based system to provide electrical contacts and feed-through for the thermocouples and gas streams. The tubular assembly with the electrochemical cell is placed inside the tubular steel shell and fixed with VCA-Swagelok and graphite connections to seal the internal chamber from the external chamber.

A thermocouple was placed inside the tubular cell to optimize temperature control. An alumina multibore liner was placed inside the tube to feed the gas from the capped side of the tube. Two copper wires were inserted into this alumina multibore liner as internal current collectors. Nickel wool was wrapped around the alumina multibore liner to ensure contact between the ceramic membrane and the copper wires. The outer tube current collector was made by wrapping copper wire around the ceramic membrane. The setup is equipped with different mass-flow controllers that allow working in different atmospheres, a water bubbler, and two back-pressure regulators (BPR) to operate at up to 30-bar pressure. The gas outlet in the inner chamber (reaction chamber) was analyzed using a Micro-GC 490 (Agilent) gas chromatograph equipped with Molsieve 5A and PoraPlot-Q glass capillary modules.

CO₂ conversion and the selectivity of the different products were evaluated on a carbon basis. First, the molar concentration of the different detected compounds was obtained from the chromatographic areas and the response factors (calibration curves and response factors are shown in [Figure S1](#)). The CO₂ conversion (X_{CO_2}) was calculated using [Equation 7](#), where $n_{CO_2}^{in}$ and $n_{CO_2}^{out}$ are the CO₂ molar flow rates in the inlet and the outlet of the inner chamber, respectively:

$$X_{CO_2} = \frac{n_{CO_2}^{in} - n_{CO_2}^{out}}{n_{CO_2}^{in}} \cdot 100 \quad (\text{Equation 7})$$

Product selectivity (CH₄ and CO) was calculated by applying [Equation 8](#), where n_i is the corresponding product molar flow rate, and n_{CO_2R} is the molar flow of the methane reacted ([Equation 9](#)). Finally, product yield is obtained by using [Equation 10](#):

$$S_i = \frac{n_i}{n_{CO_2R}} \cdot 100 \quad (\text{Equation 8})$$

$$n_{CO_2R} = n_{CO_2}^{in} - n_{CO_2}^{out} \quad (\text{Equation 9})$$

$$Y_i = \frac{S_i \cdot X_{CO_2}}{100} \quad (\text{Equation 10})$$

EIS in a range of frequencies from 1 MHz to 0.03 Hz and an alternating current (AC) signal of 30 mV and i-V curves were recorded using Solartron 1470E equipped with a 1455A frequency response analyzer (FRA) module and an Autolab potentiostat with a FRA32M module. To analyze and fit the impedance spectra, the ZView software was employed. In contrast, computing the DRTs from impedance spectroscopy data was done by a MATLAB open code toolbox.⁴²

Protonic electrochemical reactor (PER) experiments

Methanation experiments were conducted in the reactor setup described above. All experiments were carried out at 450°C and pressure from 1–30 bar. Two different

tubular cells were employed for the study; the first was operated up to 10 bar, and the second worked in the experiments performed from 10–30 bar. The different experiments carried out with the two cells (C1 and C2) are summarized in Tables S1 and S2.

Both cells' electrochemical characterizations were compared to investigate their reproducibility and electrochemical performance (Figure S1). For all experiments, the gas mixture fed to the external chamber was composed of 30 mL min⁻¹ of N₂ and 40 mL min⁻¹ of H₂ humidified at room temperature (2.5% H₂O). In the case of the internal chamber, different flows were employed, depending on the operation mode: H₂ pumping evaluation or CO₂ conversion reaction tests. In the case of the H₂ pumping evaluation, a dry atmosphere composed of 10 mL min⁻¹ H₂ and 80 mL min⁻¹ N₂ or 80 mL min⁻¹ N₂ was fed. For the methanation experiments, 150 mL min⁻¹ of a water-free atmosphere composed of CO₂, He and Ar was fed to the reaction chamber. Two gas cylinders were used during the experiments; one with a mixture of 5% CO₂ and 10% He in Ar and the other with a mixture of 15% CO₂ and 10% He in Ar. He was employed as a leak tracer and analytic internal standard. The H₂/CO₂ ratio was controlled by varying the applied current density. The CO₂ feed rate was maintained constant in the inner chamber of the protonic cell. Then, by increasing the current density applied to the cell, the H₂/CO₂ ratio was tuned because H₂ injection is proportional to the current density (considering 100% ηF). Previous to the reaction step, the H₂ flow rate was evaluated under a CO₂-free sweep-gas stream. These results allow experimental calculation of the current density needed to maintain the different ratios during the reaction. In addition, during the methanation experiment, the experimental molar flows (determined by gas chromatography [GC]) of the produced CH₄ and CO and the remaining (unreacted) H₂ in the inner chamber allows us to quantify the reached H₂/CO₂ ratio. This ratio is also compared with the previous H₂ pumping results under CO₂-free atmospheres.

Postmortem analysis

The microstructure of the electrodes and the electrode-electrolyte interface after the reaction tests was investigated by field-emission (FE) SEM (Carl Zeiss Ultra 55) before and after the electrochemical tests. Possible coke deposition on the internal electrode was evaluated by Raman spectroscopy with a Renishaw Raman spectrometer (New Mills, UK). Analyses were conducted at room temperature with a 514-nm laser equipped with an Olympus microscope and a charge-coupled device (CCD) detector. The C2 cell was also characterized by XRD and XRF spectroscopy. The XRD measurements were carried out by a PANalytical Cubix fast diffractometer using Cu Kα_{1,2} radiation (λ_{α1} = 1.5406 Å, λ_{α2} = 1.5444 Å, I₂/I₁ = 0.5) and an X'Celerator detector in Bragg-Brentano geometry. The XRD patterns were recorded from 2θ = 15°–100° and analyzed using X'Pert Highscore Plus software. The materials were measured at room temperature in an XRF spectrometer (Zetium 4 kV, provided by Malvern-Panalytical) equipped with an X-ray source with an Rh cathode. Measurements of the powder samples were performed under a He atmosphere.

SUPPLEMENTAL INFORMATION

Supplemental information can be found online at <https://doi.org/10.1016/j.checat.2023.100766>.

ACKNOWLEDGMENTS

This study has received European Union Horizon 2020 Research and Innovation funding under grant agreement 838077 (eCOCO₂ project) and financial support

from the Spanish Government (PID2022-139663OB-I00, PRE2019-090959, and CEX2021-001230-S funded by MCIN/AEI/10.13039/501100011033) and MCIN with funding from NextGenerationEU (PRTR-C17.11) within the Planes Complementarios con CCAA (Area of Green Hydrogen and Energy) and was carried out in the CSIC Interdisciplinary Thematic Platform (PTI+) Transición Energética Sostenible+ (PTI-TRANSENER+). Support from Camilla Vigen (CoorsTek Membrane Sciences) with manufacture of tubular cells is gratefully acknowledged.

AUTHOR CONTRIBUTIONS

Conceptualization, S.E., L.A., J.M.S., and T.N.; methodology, D.C.-M., L.A., S.E., A.M.D., I.Q., and A.M.; investigation, I.Q., L.A., S.E., and A.M.D.; writing – original draft, S.E., L.A., and I.Q.; writing – review & editing, J.M.S., T.N., S.E., A.M., L.A., and A.M.D.; funding acquisition, J.M.S. and T.N.; resources and supervision, J.M.S., T.N., and S.E.

DECLARATION OF INTERESTS

The authors declare no competing interests.

Received: May 27, 2023

Revised: July 18, 2023

Accepted: September 3, 2023

Published: September 27, 2023

REFERENCES

- Panzone, C., Philippe, R., Chappaz, A., Fongarland, P., and Bengaouer, A. (2020). Power-to-Liquid catalytic CO₂ valorization into fuels and chemicals: Focus on the Fischer-Tropsch route. *J. CO₂ Util.* 38, 314–347. <https://doi.org/10.1016/j.jcou.2020.02.009>.
- Vázquez, F.V., Koponen, J., Ruuskanen, V., Bajamundi, C., Kosonen, A., Simell, P., Ahola, J., Frilund, C., Elfving, J., Reinikainen, M., et al. (2018). Power-to-X technology using renewable electricity and carbon dioxide from ambient air: SOLETAIR proof-of-concept and improved process concept. *J. CO₂ Util.* 28, 235–246. <https://doi.org/10.1016/j.jcou.2018.09.026>.
- Straka, P. (2021). A comprehensive study of Power-to-Gas technology: Technical implementations overview, economic assessments, methanation plant as auxiliary operation of lignite-fired power station. *J. Clean. Prod.* 311, 127642. <https://doi.org/10.1016/j.jclepro.2021.127642>.
- Ghaib, K., and Ben-Fares, F.Z. (2018). Power-to-Methane: A state-of-the-art review. *Renew. Sustain. Energy Rev.* 81, 433–446. <https://doi.org/10.1016/j.rser.2017.08.004>.
- Rasmussen, M.G., Andresen, G.B., and Greiner, M. (2012). Storage and balancing synergies in a fully or highly renewable pan-European power system. *Energy Pol.* 51, 642–651. <https://doi.org/10.1016/j.enpol.2012.09.009>.
- Reznicek, E.P., and Braun, R.J. (2020). Reversible solid oxide cell systems for integration with natural gas pipeline and carbon capture infrastructure for grid energy management. *Appl. Energy* 259, 114118. <https://doi.org/10.1016/j.apenergy.2019.114118>.
- Wendel, C.H., Kazempoor, P., and Braun, R.J. (2016). A thermodynamic approach for selecting operating conditions in the design of reversible solid oxide cell energy systems. *J. Power Sources* 301, 93–104. <https://doi.org/10.1016/j.jpowsour.2015.09.093>.
- Becker, W.L., Penev, M., and Braun, R.J. (2019). Production of synthetic natural gas from carbon dioxide and renewably generated hydrogen: A techno-economic analysis of a power-to-gas strategy. *J. Energy Resour. Technol.* 141. <https://doi.org/10.1115/1.4041381>.
- McKenna, R.C., Bchini, Q., Weinand, J.M., Michaelis, J., König, S., Köppel, W., and Fichtner, W. (2018). The future role of Power-to-Gas in the energy transition: Regional and local techno-economic analyses in Baden-Württemberg. *Appl. Energy* 212, 386–400. <https://doi.org/10.1016/j.apenergy.2017.12.017>.
- Gruber, M., Weinbrecht, P., Biffar, L., Harth, S., Trimis, D., Brabandt, J., Posdziech, O., and Blumentritt, R. (2018). Power-to-Gas through thermal integration of high-temperature steam electrolysis and carbon dioxide methanation - Experimental results. *Fuel Process. Technol.* 181, 61–74. <https://doi.org/10.1016/j.fuproc.2018.09.003>.
- Ashok, J., Pati, S., Hongmanorom, P., Tianxi, Z., Junmei, C., and Kawi, S. (2020). A review of recent catalyst advances in CO₂ methanation processes. *Catal. Today* 356, 471–489. <https://doi.org/10.1016/j.cattod.2020.07.023>.
- Rahmani, S., Rezaei, M., and Meshkani, F. (2014). Preparation of highly active nickel nanocrystalline γ -Al₂O₃ for CO₂ methanation. *J. Ind. Eng. Chem.* 20, 1346–1352. <https://doi.org/10.1016/J.JIEC.2013.07.017>.
- Takenaka, S., Shimizu, T., and Otsuka, K. (2004). Complete removal of carbon monoxide in hydrogen-rich gas stream through methanation over supported metal catalysts. *Int. J. Hydrogen Energy* 29, 1065–1073. <https://doi.org/10.1016/J.IJHYDENE.2003.10.009>.
- Gao, J., Wang, Y., Ping, Y., Hu, D., Xu, G., Gu, F., and Su, F. (2012). A thermodynamic analysis of methanation reactions of carbon oxides for the production of synthetic natural gas. *RSC Adv.* 2, 2358–2368. <https://doi.org/10.1039/C2RA00632D>.
- Lee, W.J., Li, C., Prajitno, H., Yoo, J., Patel, J., Yang, Y., and Lim, S. (2021). Recent trend in thermal catalytic low temperature CO₂ methanation: A critical review. *Catal. Today* 368, 2–19. <https://doi.org/10.1016/j.cattod.2020.02.017>.
- Vogt, C., Monai, M., Kramer, G.J., and Weckhuysen, B.M. (2019). The renaissance of the Sabatier reaction and its applications on Earth and in space. *Nat. Catal.* 2, 188–197. <https://doi.org/10.1038/s41929-019-0244-4>.
- Li, L., Li, H., Tian, Q., Ge, B., Xu, X., Chi, Y., Zhao, H., Liu, Y., Jia, N., Zhou, T., et al. (2022). Research Progress and Reaction Mechanism of CO₂ Methanation over Ni-Based Catalysts at Low Temperature: A Review. *Catalysts* 12, 244. <https://doi.org/10.3390/CATAL12020244>.
- Dębek, R., Azzolina-Jury, F., Travert, A., and Mauge, F. (2019). A review on plasma-catalytic

- methanation of carbon dioxide – Looking for an efficient catalyst. *Renew. Sustain. Energy Rev.* 116, 109427. <https://doi.org/10.1016/j.rser.2019.109427>.
19. Zhu, Y., Chen, S., Fang, S., Li, Z., Wang, C., and Hu, Y.H. (2021). Distinct Pathways in Visible-Light Driven Thermo-Photo Catalytic Methane Conversion. *J. Phys. Chem. Lett.* 12, 7459–7465. https://doi.org/10.1021/ACS.JPCLETT.1C02053/ASSET/IMAGES/LARGE/JZ1C02053_0003.JPEG.
 20. Kattel, S., Liu, P., and Chen, J.G. (2017). Tuning Selectivity of CO₂ Hydrogenation Reactions at the Metal/Oxide Interface. *J. Am. Chem. Soc.* 139, 9739–9754. https://doi.org/10.1021/JACS.7B05362/ASSET/IMAGES/LARGE/JA-2017-05362S_0014.JPEG.
 21. Weatherbee, G., and Bartholomew, C.H. (1981). Hydrogenation of CO₂ on group VIII metals: I. Specific activity of NiSiO₂. *J. Catal.* 68, 67–76. [https://doi.org/10.1016/0021-9517\(81\)90040-3](https://doi.org/10.1016/0021-9517(81)90040-3).
 22. Peebles, D.E., Goodman, D.W., and White, J.M. (1983). Methanation of carbon dioxide on Ni(100) and the effects of surface modifiers. *J. Phys. Chem.* 87, 4378–4387. https://doi.org/10.1021/J100245A014/ASSET/J100245A014.FP.PNG_V03.
 23. Nolen, M.A., Tacey, S.A., Kwon, S., and Farberow, C.A. (2023). Theoretical assessments of CO₂ activation and hydrogenation pathways on transition-metal surfaces. *Appl. Surf. Sci.* 637, 157873. <https://doi.org/10.1016/j.apsusc.2023.157873>.
 24. Avanesian, T., Gusmão, G.S., and Christopher, P. (2016). Mechanism of CO₂ reduction by H₂ on Ru(0 0 0 1) and general selectivity descriptors for late-transition metal catalysts. *J. Catal.* 343, 86–96. <https://doi.org/10.1016/j.jcat.2016.03.016>.
 25. Bausá, N., Escolástico, S., and Serra, J.M. (2019). Direct CO₂ conversion to syngas in a BaCe_{0.2}Zr_{0.7}Y_{0.1}O_{3-δ}-based proton-conducting electrolysis cell. *J. CO₂ Util.* 34, 231–238. <https://doi.org/10.1016/j.jcou.2019.05.037>.
 26. Malerød-Fjeld, H., Clark, D., Yuste-Tirados, I., Zanón, R., Catalán-Martínez, D., Beeaff, D., Morejudo, S.H., Vestre, P.K., Norby, T., Haugrud, R., et al. (2017). Thermo-electrochemical production of compressed hydrogen from methane with near-zero energy loss. *Nat. Energy* 2, 923–931. <https://doi.org/10.1038/s41560-017-0029-4>.
 27. Pan, Z., Duan, C., Pritchard, T., Thatte, A., White, E., Braun, R., O'Hayre, R., and Sullivan, N.P. (2022). High-yield electrochemical upgrading of CO₂ into CH₄ using large-area protonic ceramic electrolysis cells. *Appl. Catal., B* 307, 121196. <https://doi.org/10.1016/j.apcatb.2022.121196>.
 28. Xie, K., Zhang, Y., Meng, G., and Irvine, J.T.S. (2011). Direct synthesis of methane from CO₂/H₂O in an oxygen-ion conducting solid oxide electrolyser. *Energy Environ. Sci.* 4, 2218–2222. <https://doi.org/10.1039/c1ee01035b>.
 29. Luo, Y., Li, W., Shi, Y., Cao, T., Ye, X., Wang, S., and Cai, N. (2015). Experimental Characterization and Theoretical Modeling of Methane Production by H₂O/CO₂ Co-Electrolysis in a Tubular Solid Oxide Electrolysis Cell. *J. Electrochem. Soc.* 162, F1129–F1134. <https://doi.org/10.1149/2.0171510jes>.
 30. Li, G., Gou, Y., Qiao, J., Sun, W., Wang, Z., and Sun, K. (2020). Recent progress of tubular solid oxide fuel cell: From materials to applications. *J. Power Sources* 477, 228693. <https://doi.org/10.1016/j.jpowsour.2020.228693>.
 31. Ni, M., Leung, M.K., and Leung, D.Y. (2008). Electrochemical modeling of hydrogen production by proton-conducting solid oxide steam electrolyzer. *Int. J. Hydrogen Energy* 33, 4040–4047. <https://doi.org/10.1016/j.ijhydene.2008.05.065>.
 32. Pirou, S., Wang, Q., Khajavi, P., Georgolamprou, X., Ricote, S., Chen, M., and Kiebach, R. (2022). Planar proton-conducting ceramic cells for hydrogen extraction: Mechanical properties, electrochemical performance and up-scaling. *Int. J. Hydrogen Energy* 47, 6745–6754. <https://doi.org/10.1016/j.ijhydene.2021.12.041>.
 33. Wang, Q., Luo, T., Tong, Y., Dai, M., Miao, X.Y., Ricote, S., Zhan, Z., and Chen, M. (2022). Large-area protonic ceramic cells for hydrogen purification. *Sep. Purif. Technol.* 295, 121301. <https://doi.org/10.1016/j.seppur.2022.121301>.
 34. Meng, X., Tong, Y., Luo, T., Cui, C., Wang, Y., Wang, S., Peng, R., Xie, B., Chen, C., Zhan, Z., et al. (2020). Protonic Ceramic Electrochemical Cell for Efficient Separation of Hydrogen. *ACS Appl. Mater. Interfaces* 12, 25809–25817. <https://doi.org/10.1021/acsami.0c04024>.
 35. Robinson, S., Manerfino, A., and Grover Coors, W. (2013). Galvanic hydrogen pumping in the protonic ceramic perovskite BaCe_{0.2}Zr_{0.7}Y_{0.1}O_{3-δ}. *J. Membr. Sci.* 446, 99–105. <https://doi.org/10.1016/j.memsci.2013.06.026>.
 36. Patki, N.S., Manerfino, A., Way, J.D., and Ricote, S. (2018). Galvanic hydrogen pumping performance of copper electrodes fabricated by electrodeless plating on a BaZr_{0.9-x}Ce_xY_{0.1}O_{3-δ} proton-conducting ceramic membrane. *Solid State Ionics* 317, 256–262. <https://doi.org/10.1016/j.ssi.2018.01.031>.
 37. Morejudo, S.H., Zanón, R., Escolástico, S., Yuste-Tirados, I., Malerød-Fjeld, H., Vestre, P.K., Coors, W.G., Martínez, A., Norby, T., Serra, J.M., and Kjølseth, C. (2016). Direct conversion of methane to aromatics in a catalytic co-ionic membrane reactor. *Science* 353, 563–566. <https://doi.org/10.1126/science.aag0274>.
 38. Clark, D., Malerød-Fjeld, H., Budd, M., Yuste-Tirados, I., Beeaff, D., Aamodt, S., Nguyen, K., Ansaloni, L., Peters, T., Vestre, P.K., et al. (2022). Single-step hydrogen production from NH₃, CH₄, and biogas in stacked proton ceramic reactors. *Science* 376, 390–393. <https://doi.org/10.1126/science.abj3951>.
 39. Xie, K., Zhang, Y., Meng, G., and Irvine, J.T.S. (2011). Electrochemical reduction of CO₂ in a proton conducting solid oxide electrolyser. *J. Mater. Chem.* 21, 195–198. <https://doi.org/10.1039/c0jm02205e>.
 40. Duan, C., Kee, R., Zhu, H., Sullivan, N., Zhu, L., Bian, L., Jennings, D., and O'Hayre, R. (2019). Highly efficient reversible protonic ceramic electrochemical cells for power generation and fuel production. *Nat. Energy* 4, 230–240. <https://doi.org/10.1038/s41560-019-0333-2>.
 41. Vøllestad, E., Strandbakke, R., Tarach, M., Catalán-Martínez, D., Fontaine, M.L., Beeaff, D., Clark, D.R., Serra, J.M., and Norby, T. (2019). Mixed proton and electron conducting double perovskite anodes for stable and efficient tubular proton ceramic electrolyzers. *Nat. Mater.* 18, 752–759. <https://doi.org/10.1038/s41563-019-0388-2>.
 42. Wan, T.H., Saccoccio, M., Chen, C., and Ciucci, F. (2015). Influence of the Discretization Methods on the Distribution of Relaxation Times Deconvolution: Implementing Radial Basis Functions with DRTtools. *Electrochim. Acta* 184, 483–499. <https://doi.org/10.1016/j.electacta.2015.09.097>.
 43. Herradon, C., Le, L., Meisel, C., Huang, J., and Chmura, C. (2022). Proton-conducting Ceramics for Water Electrolysis and Hydrogen Production at Elevated Pressure, pp. 1–12. <https://doi.org/10.3389/fenrg.2022.1020960>.
 44. Sumi, H., Shimada, H., Yamaguchi, Y., Mizutani, Y., Okuyama, Y., and Amezawa, K. (2021). Comparison of electrochemical impedance spectra for electrolyte-supported solid oxide fuel cells (SOFCs) and protonic ceramic fuel cells (PCFCs). *Sci. Rep.* 11, 10622–10629. <https://doi.org/10.1038/s41598-021-90211-9>.
 45. Le, L.Q., Meisel, C., Hernandez, C.H., Huang, J., Kim, Y., O'Hayre, R., and Sullivan, N.P. (2022). Performance degradation in proton-conducting ceramic fuel cell and electrolyzer stacks. *J. Power Sources* 537, 231356. <https://doi.org/10.1016/j.jpowsour.2022.231356>.
 46. Escorihuela, S., Cerdá-Moreno, C., Weigelt, F., Remiro-Buenamañana, S., Escolástico, S., Tena, A., Shishatskiy, S., Brinkmann, T., Chica, A., and Serra, J.M. (2022). Intensification of catalytic CO₂ methanation mediated by in-situ water removal through a high-temperature polymeric thin-film composite membrane. *J. CO₂ Util.* 55, 1–9. <https://doi.org/10.1016/j.jcou.2021.101813>.
 47. Wang, Y., Zhang, H., Cao, J., Xu, K., Pei, K., and Chen, Y. (2022). Highly selective reduction of CO₂ through a protonic ceramic electrochemical cell. *J. Power Sources* 524, 231101. <https://doi.org/10.1016/j.jpowsour.2022.231101>.